Available online at www.sciencedirect.com

ScienceDirect

ELSEVIER

International Journal of Heat and Mass Transfer 50 (2007) 1141–1154

International Journal of HEAT and MASS TRANSFER

www.elsevier.com/locate/ijhmt

On the thermal performance of wire-screen meshes as heat exchanger material

J. Xu [a], J. Tian [a], T.J. Lu [a,b,*], H.P. Hodson [a]

[a] *Department of Engineering, University of Cambridge, Cambridge CB2 1PZ, UK*
[b] *MOE Key Laboratory for Strength and Vibration, School of Aerospace, Xi'an Jiaotong University, Xian 710049, PR China*

Received 27 May 2005
Available online 20 December 2006

Abstract

Due to large number of design parameters, numerical analysis is inevitable for heat exchanger design with wire-screen structures. This paper establishes a direct simulation method to study the laminar flow and heat transfer at the pore level. The experiment validation proves this analysis is reliable. For both the pressure drop and heat transfer characteristics, various configurations of wire-screen meshes are investigated, where water has been used as coolant. Material properties difference such as conductivity and heat capacity ratios of the two phases are evaluated. Structure porosity is also quantified and it is found that there exists an optimised porosity for the thermal performance. The properties of water at 20 °C are used for the fluid phase.

1. Introduction

Metallic wire-screen meshes have been widely used in refrigeration, chemical reaction, food processing, solar energy collection, heat dissipation, combustion, and other applications [1–5]. Due to the large values of surface area density (defined as wetted surface area per volume), these structures are found to be effective in dissipating heat within a limited design space [6,7]. Much attention has hence been drawn to study the hydraulic and thermal performance of these structures.

Ergun [8], Armour and Cannon [9] and Sodre and Parise [10] experimentally investigated the flow through the wire-screen structures; with focus placed on hydraulic characteristics, the determination of frictional factors was discussed. Richards and Robinson [4] studied the effect of wire shapes on pressure drop and found that the friction factor depends both on structure porosities and the cross-section shapes of wires, thus proposed the concept of effective porosity for a general mesh structure. Tian et al. [6] measured both the pressure loss and heat transfer performance characteristics of brazed woven mesh structures in forced air convection. They evaluated the effect of different cell shapes and different orientations of the structure, and found that the pressure drop is dominated by form drag while solid conduction and fluid convection are both important for the heat transfer. Furthermore, it was found that for a fixed surface area density there exists an optimal porosity (~0.8) for maximal heat dissipation. For solar energy collection, Kolb et al. [2] found that the wire-screen matrix yields an improved thermal performance with higher heat transfer rates and smaller friction losses compared to traditional flat-plate design. They also suggested that a simulation model is needed for optimisation design because of the large number of design and operation parameters.

To simulate fluid flow and heat transfer cross wire-screen meshes, many researchers treated these structures as porous media. An effective thermal conductivity needs to be determined for the transformed pseudo-single phase in this treatment. By considering only the conduction of wire-screen layers saturated with fluid, Hsu et al. [11]

---

[*] Corresponding author. Address: Department of Engineering, University of Cambridge, Cambridge CB2 1PZ, UK. Tel.: +86 29 82665600; fax: +86 29 83234781.

E-mail addresses: tjlu@mail.xjtu.edu.cn, TJL21@cam.ac.uk (T.J. Lu).

0017-9310/$ - see front matter © 2006 Elsevier Ltd. All rights reserved.
doi:10.1016/j.ijheatmasstransfer.2006.05.044

Nomenclature

A	heating area, m^2
c_p, c	specific heat, $\mathrm{J\,kg^{-1}\,K^{-1}}$
c_{int}	skin friction coefficient along strut surface, m^{-1}
d	wire diameter, m
d_p	unit cell diameter, m
w	the width of wire-screen aperture, m
h_{sf}	interfacial heat transfer coefficients, $\mathrm{W\,m^{-2}\,K^{-1}}$
$\boldsymbol{n}$	interfacial surface normal vector
f_{H}	friction factor, m^{-1}
L	the length of the testing samples, m
H	the height of the channel, m
h_{int}	surface heat transfer coefficient along strut surface, $\mathrm{W\,m^{-2}\,K^{-1}}$
R_{open}	open area ratio
q	heat flux, $\mathrm{W\,m^{2}}$
Q	heat input from bottom facesheet, W
T	temperature, K
U	velocity, $\mathrm{m\,s^{-1}}$
u_i	velocity component, $\mathrm{m\,s^{-1}}$
$\boldsymbol{V}$	velocity vector, $\mathrm{m\,s^{-1}}$
a_{sf}	surface area density, m^{-1}
ε	porosity
λ	fluid/solid thermal conductivity ratio
μ	molecular viscosity, $\mathrm{kg\,m^{-1}\,s^{-1}}$
v	kinetic viscosity, $\mathrm{m^2\,s^{-1}}$
ρ	density, $\mathrm{kg\,m^{-3}}$
k	thermal conductivity, $\mathrm{W\,m^{-1}\,K^{-1}}$
ΔP	pressure drop, Pa

Subscripts

eff	effective
ref	reference
f	fluid
s	solid
m	mean
in	inlet
out	outlet
int	interfacial

studied the effective thermal conductivity of wire screens at the stagnant situation. Wirtz and co-workers [12,13] also used a conduction model to calculate the effective conductivity: their predictions agree with experimental measurements for airflow, as the fluid conductivity is insignificant. Chang [14] established the correlations between effective thermal conductivity and structure porosity. Using directly friction factor and heat transfer correlations for packed bed of spheres, Paul and Saini [15] optimised the design parameters for wire-screen matrixes.

General analytical models have been developed from the porous medium prototype. Depending on the efficiency of energy exchange between solid and fluid phases, these models can be catalogued as one-energy-equation models (see Refs. [16,17]) and two-energy-equation models (see Refs. [18,19]). The former assumes that a thermal equilibrium between the two phases is established locally due to efficient thermal communication, whilst the latter acknowledges the local temperature difference between the two phases and employs separate differential equations governing the energy transportation in the two phases. Further studies using the above approach can be found in Refs. [20–25]. Results presented in [20,21] show that non-Darcy effect is important for fluid flow through wire screens. Duprat and Lopez [22] found that, for fixed heat transfer efficiency, wire screens cover a wider range of gauges than packed bed of spheres. Ahmad et al. [23] concluded that copper woven screens are promising thermal energy absorber matrices for solar energy collection. Using experimental data for wire screens, Ozdemir and Ozguc [24] determined the various constants in the porous medium model and found the model is valid only if representative element volumes are carefully chosen. For the near wall region in particular, an artificial variant porosity has to be introduced to adapt the model prediction to the experimental data. This effect is generally called the channel effect and was originally noticed by Mehta and Hawley [25]. Vafai and co-workers [26,19] analytically investigated the channelling effect and proposed an exponent function for porosity values near the sidewall; the proposed porosity seemed able to capture the peak velocity adjacent to the sidewall observed in packed bed of spheres. Ozdemir and Ozguc [27] experimentally determined the porosity values for each layer of a wire screens structure, and confirmed that this exponentially damping porosity is necessary in the models in order to count for the sidewall effect.

Nearly all of the previous modelling attempts were entirely based on a porous model prototype, and few numerical simulations have been carried out to specify the large number of design and operation parameters involved. In these models, the effective thermal conductivities were determined either using data from packed bed or from wire screens with fluid convection ignored. Near a sidewall, an artificial variable porosity has to be introduced so that representative element volumes (REV) can be reasonably chosen. Although this variable porosity leads to a peak velocity near the adjacent wall, there is no reported experimental evidence on this velocity peak for wire screens. Even for packed bed of spheres, Hunt and Tian [16] observed that the cross-flow velocity profile is close to a parabolic one. Also, the variable porosity treatment predicts a creep-like flow field similar to a Darcian flow, although it has been reported that non-Darcy effects cannot be ignored for flow across wire screens. Porous medium models have been shown to be suitable for stochastic structures such as packed bed of spheres, metal foams, etc. [28], but for wire-screen meshes, lattice frame materials [29,30] and other porous media having periodic microstructures a different approach is perhaps more fruitful in capturing the precisely periodic flow and temperature fields and hence predicting the overall performance [29].

This paper establishes a direct numerical simulation on the fluid flow and heat transfer characteristics at the structure pore level, overcome the shortcoming of the above-mentioned shortcomings of porous medium modelling. The experiment rig is also set up to measure the overall pressure drop and Nusselt number data of the wire-screen structure, so that the numerical analysis is validated. The geometry domain is reasonably simplified for an affordable numerical model. The conjugate heat transfer between solid and fluid phases is considered without any modelling. Different parameters are evaluated for thermal performance comparisons.

2. Experiment procedures

2.1. Fabrication of test sample

The test section for forced water convection experiment (see next section for details), the test sample used and the arrangements of temperature and pressure probes are shown in Fig. 1a, b and c, respectively, whilst the textile-based approach for the synthesis of wire-screen laminates is illustrated in Fig. 2. The wire alloy is C110000 copper (99.95Cu–0.04O) with a density of $\rho_s = 8.89\ \mathrm{g/cm^3}$ and a thermal conductivity of $k_s \approx 385\ \mathrm{W/(mK)}$ at ambient conditions. Prototype sandwich heat sink with laminated textile cores of plain woven copper cloth (obtained from GDC/City Wire Cloth Co., Fontana, CA) is fabricated using the brazing method.

For the brazing operation, individual laminae are stacked, with alignment achieved using threaded guide pins to align all openings. The laminae are stacked peak-to-peak to ensure a regular structure. A small compressive pressure is then applied to the guide pins to maintain contact at the peak-to-peak nodes. The entire assembly is then dipped into a viscous brazing paste of CuproBraz®. By using high strength and high conductivity copper and copper alloys it is possible to manufacture light, strong, efficient and compact heat exchangers at a low cost with this environmentally friendly process. The braze coated assemblies are air dried in a warming oven then transferred to a vacuum furnace and heated under a partial pressure of argon (0.25 Torr) at a rate of 30 °C/min to 650 °C and held for 15 min, followed by a rapid furnace cool. Finally, the brazed core assemblies are machined to size and solid copper facesheets are attached using the same brazing process.

The sandwich panels thus created can be designed to carry structural load at minimum weight, while simultaneously allowing fluid passage for cooling or other purposes.

The characteristic parameters of the test sample used in the experiment are summarised in Table 1.

2.2. Experimental setup

The experiment rig for pressure drop and heat transfer measurement contains four main components: water supply system, test section, heating arrangement and data acquisition. At low flow rates, water is supplied directly by a high-positioned reservoir and a valve controls the flow rate; after flowing through the test section water goes to a low-positioned reservoir for mass flux measurement or is drained off. At relatively high flow rates, water is supplied by a circular system: the heated water after the test section is cooled down via a heat exchanger before it is pumped for inflow again. The mean water velocity in the experiments varies from 0.04 to 0.4 m/s.

The sandwich heat sink has height H, width W and length L (Table 1). A constant heat flux is supplied at the bottom facesheet and the top facesheet is thermally insulated (Fig. 1a). For heat input, nickel–chromium (Cr20 Ni80) plate with thickness of 0.1 mm is machined into snake shape and electrically heated; the input voltage is recorded to calculate the wall heat flux. T-type copper–constantan thermocouples with diameter of 0.2 mm are buried into grooves on the top copper facesheet of the sandwich heat sink to measure local temperature variations. Additional thermocouples are used to measure the inlet and outlet fluid temperatures. A high-resolution manometer is used for pressure measurement. Mass flow rate is obtained using the mass weight method.

2.3. Data reduction

The Reynolds number and friction factor based on the channel height are defined as

$$Re_\mathrm{H} = \frac{\rho_\mathrm{f} u_\mathrm{m} H}{\mu_\mathrm{f}} \tag{1}$$

$$f_\mathrm{H} = \left(\frac{\Delta p}{L} \cdot H\right) \cdot \left(\frac{1}{\rho_\mathrm{f} u_\mathrm{m}^2/2}\right) \tag{2}$$

where u_m is the mean coolant velocity at the inlet of the test section, ρ_f and μ_f are the coolant density and viscosity, and $\Delta P/L$ is the pressure drop per unit length.

For heat transfer characterization, the heat transfer coefficient h and the corresponding Nusselt number Nu_H are defined as

$$h(x) = \frac{Q}{A}\frac{1}{\Delta T(x)} = \frac{q}{T_\mathrm{w}(x) - T_\mathrm{in}} \tag{3}$$

$$Nu_\mathrm{H} = \frac{h \cdot H}{k_\mathrm{f}} \tag{4}$$

where the coordinate x measures from the entrance of the test sample in the main flow direction, k_f is the thermal conductivity of the coolant, and $q = Q/A$ the input heat flux.

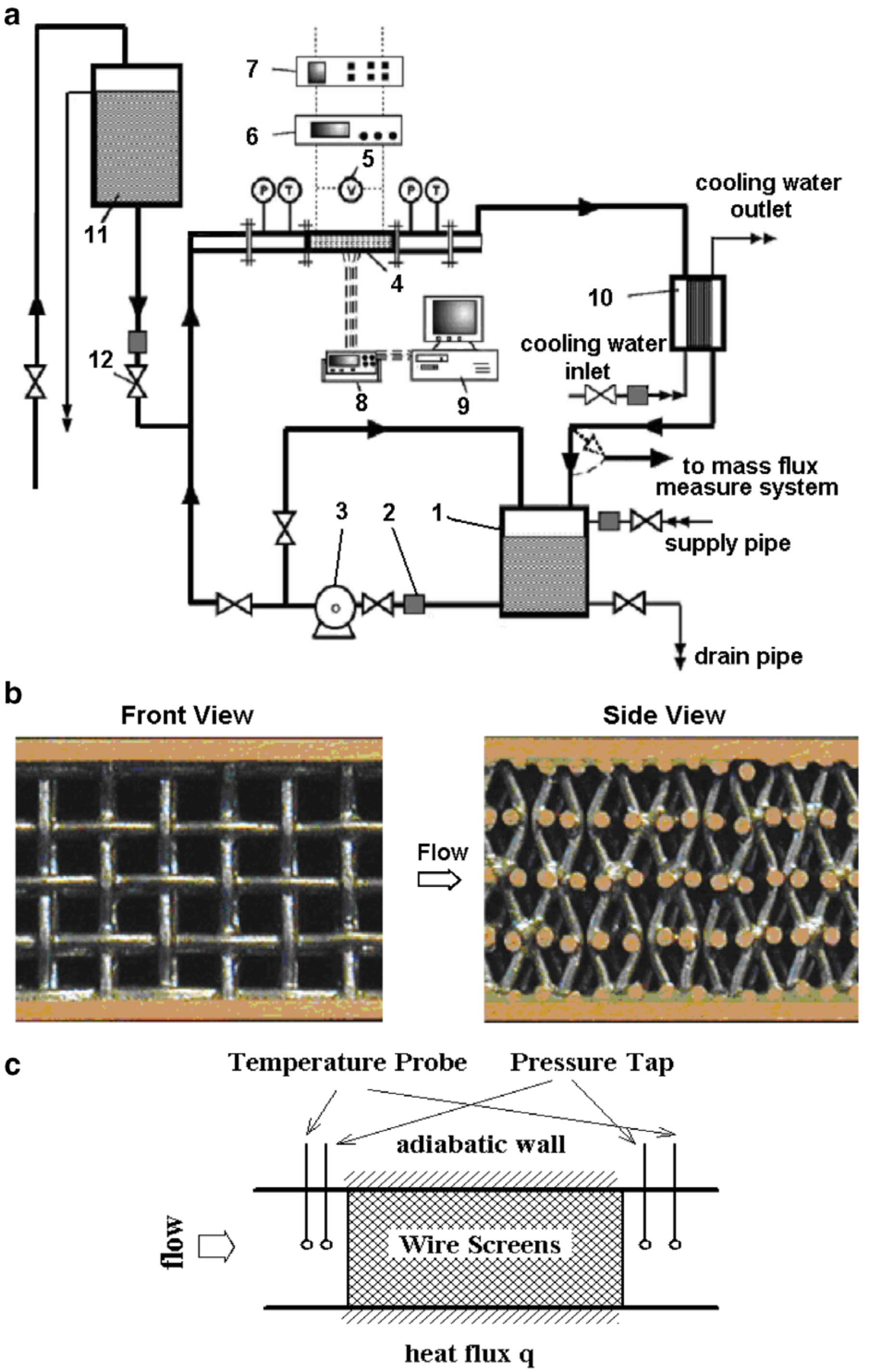

Fig. 1. Test section: (a) schematic diagram; (b) front and side view of test sample.

Here, Q is the input rate of heat, A the heating area (namely, the copper substrate area), T_w the temperature of the bottom facesheet, and T_{in} the bulk mean temperature of the coolant at inlet.

An uncertainty analysis is carried out following the method described in Coleman and Steele [31]. Within the operating temperature range of 10–20 °C, the variation in the thermal conductivity of water, k_f, is negligible, whereas its density varies less than 3% and viscosity less than 2.5%. The uncertainty in pressure drop measurement is estimated to be less than 2.5%. The uncertainty of heat balance is less than 12%. Accordingly, the uncertainties calculated from the root-square method for the Reynolds number, frictional factor, mean heat transfer coefficient and Nusselt number are estimated to be less than 4%, 4.1%, 12.4% and 12.4%, respectively.

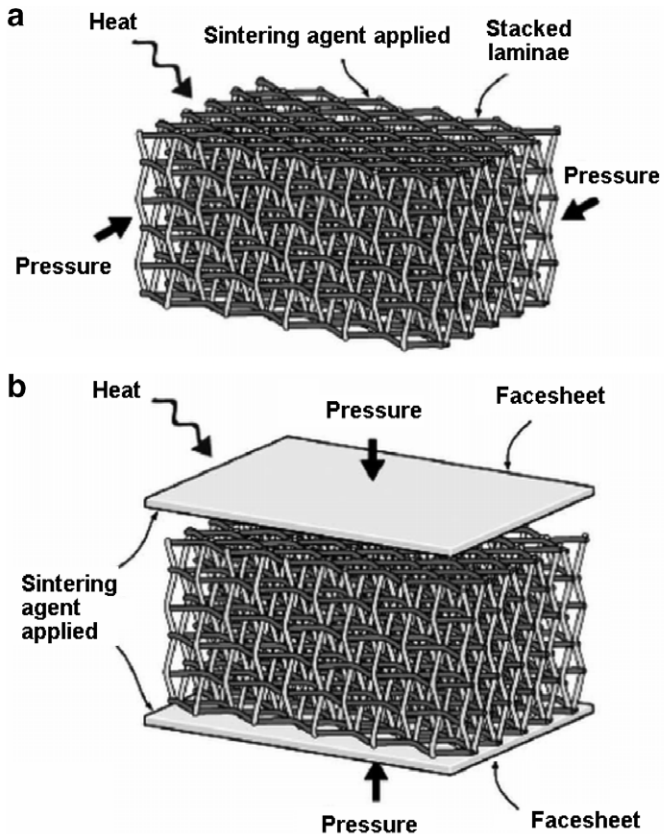

Fig. 2. Sandwich construction with textile technology: (a) a transient liquid joins the wire-mesh screen laminated at all points of contact; (b) facesheets are added to the textile core.

Table 1
Details of the sample

Diameter, d ($\times 10^{-3}$ m)	Aperture, w ($\times 10^{-3}$ m)	Channel height, H ($\times 10^{-3}$ m)	Channel width, W ($\times 10^{-3}$ m)	Channel length, L ($\times 10^{-3}$ m)
0.8	2.36	10	40	60

3. Numerical simulations

3.1. Simplifications of the geometry

During the brazing process of the test sample, small amount of solid material is attached to peak-to-peak nodes (where wires touch each other) and wire-to-facesheet joints (where some horizontal wires touch top or bottom facesheet). If the fillings being omitted and mesh screens being perfectly fabricated, the structure can be schematically shown in Fig. 3a. In the idealised geometry only the wire diameter d and the aperture w between neighbouring wires are the controlling parameters. The open ratio (i.e., ratio of void area to whole cross-sectional area from the frontal view shown in Fig. 1b) R_{open}, the structure porosity ε and the surface area density α_{sf} are determined as following:

$$R_{\text{open}} = \frac{(w/d)^2}{1+(w/d)^2} \tag{5}$$

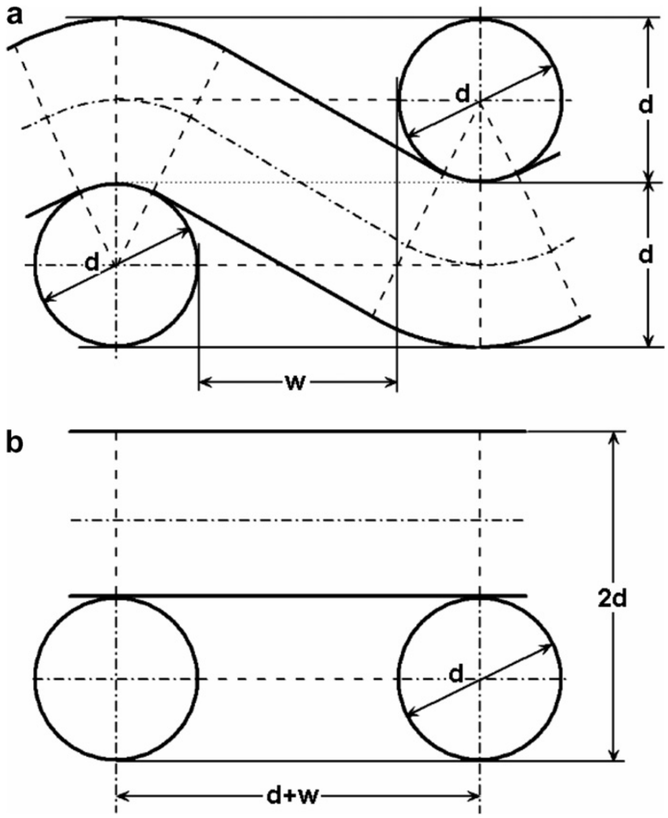

Fig. 3. Wire-screen geometry simplification: (a) idealised geometry; (b) simplified geometry.

$$\varepsilon = 1 - \frac{\pi}{4(1+w/d)} \times \frac{\sqrt{(1+w/d)^2-3} + 2\arctan\left(3\Big/\left(1+w/d+2\sqrt{(1+w/d)^2-3}\right)\right)}{1+w/d} \tag{6}$$

$$\alpha_{\text{sf}} = \frac{\pi/d}{1+w/d} \times \frac{\sqrt{(1+w/d)^2-3} + 2\arctan\left(3\Big/\left(1+w/d+2\sqrt{(1+w/d)^2-3}\right)\right)}{1+w/d} \tag{7}$$

It can be seen that the open area ratio and porosity depend only on the ratio of the ratio of aperture to diameter, w/d. Eq. (7) can be re-written as

$$\alpha_{\text{sf}} \cdot d = \frac{\pi}{1+w/d} \times \frac{\sqrt{(1+w/d)^2-3} + 2\arctan\left(3\Big/\left(1+w/d+2\sqrt{(1+w/d)^2-3}\right)\right)}{1+w/d} \tag{8}$$

so that the right-hand side is again an function of only the aperture-to-diameter ratio.

It is found that the geometry has to be simplified to generate a computationally affordable mesh. The simplification was done so that the stacked woven mesh screens become layers of wire arrays with crossed axis direction for every other layer. Consequently the idealised cell geometry for the test sample shown in Fig. 3a becomes the simplified one as illustrated in Fig. 3b, where the originally curved wires are replaced with straight ones. The diameter $d$and aperture w are remained unchanged during the simplification. As such, the open area ratio remains the same as before but the porosity and surface area density differ from before. Specifically the structure porosity becomes greater and surface area density smaller after simplification. For the simplified geometry, ε and α_{sf} are given by

$$\varepsilon = 1 - \frac{\pi}{4(1 + w/d)} \tag{9}$$

$$\alpha_{sf} \cdot d = \frac{\pi}{1 + w/d} \tag{10}$$

Eq. (10) is written similarly to Eq. (8) so that the right-hand side depends only on w/d.

To check the difference between two geometry types, with respect to their hydrodynamic and thermodynamic characteristics, the structure porosity and surface area density are plotted in Fig. 4 as functions of the aperture-to-diameter ratio w/d. For the convenience the surface area density is indirectly presented in Fig. 4b through the product $\alpha_{sf} \cdot d$. In Fig. 4, the difference reaches the maximum at the aperture-to-diameter ratio of $\sqrt{3}-1$ (the nature limit of the idealised woven geometry), for both porosity and surface area density; it monotonously decreases as the aperture-to-diameter ratio increases and becomes relatively small for an aperture-to-diameter ratio larger than 3, indicating the two geometries are close to each other, in terms of fluid flow and heat transfer behaviours. With the experimental test sample as reference, the values of porosity and surface area density for the two geometries correspondent to the sample are listed in Table 2. It is seen from Table 2 that the deviations of the simplified geometry are less than 0.8% in comparison with the idealised geometry and less than 0.5% with the experimental geometry. The nominal open area ratios are the same for all the three geometries. Since the porosity, surface area density and open area ratio are the key parameters addressing fluid flow and heat transfer in a wire-screen mesh structure, from convective heat transfer point of view, the simplified geometry of Fig. 3b may be assumed to be a good approximation of the actual geometry of Fig. 1b.

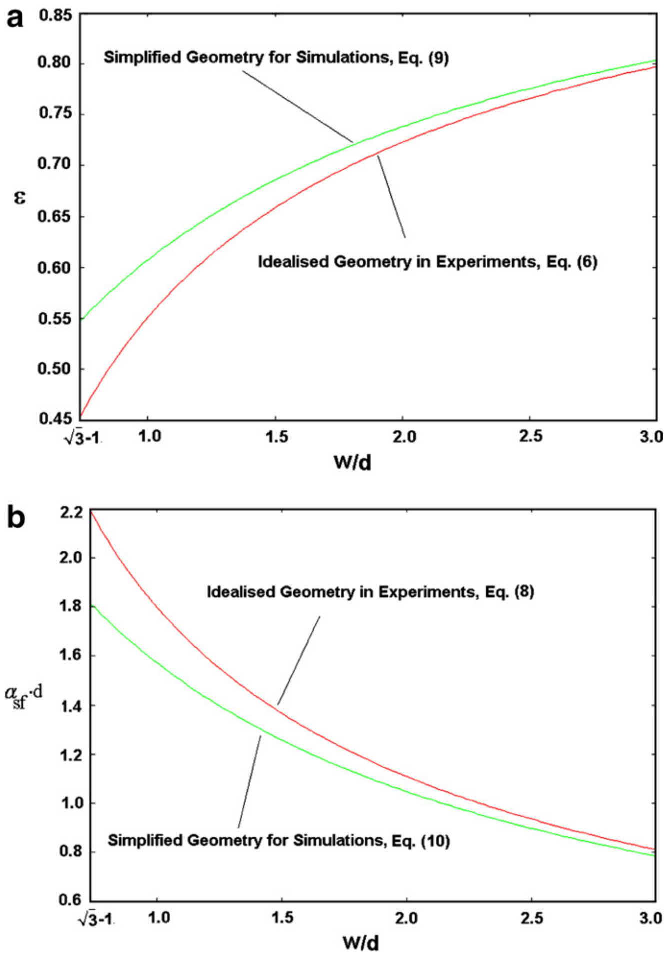

Fig. 4. Difference between idealised and simplified geometries: (a) porosity; (b) surface density.

Table 2
Geometry difference

	Real geometry	Idealised geometry	Simplified geometry	Deviation
Diameter, d ($\times 10^{-3}$ m)	0.8	0.8	0.8	
Aperture, w ($\times 10^{-3}$ m)	2.36	2.36	2.36	
Channel height, H ($\times 10^{-3}$ m)	10	10.28	10.28	
Porosity, ε	0.795	0.799	0.801	<0.8%
Surface area density, α_{sf}(m^{-1})	994	1005	998	<0.5%

It has been mentioned that the geometry shown in Fig. 3a is idealised with the solid paste remaining in the contact region during the brazing process being ignored, so that the cylindrical struts contact each other at a single point (peak-to-peak node), and some horizontal wires touch the top and bottom facesheets with a curve/line. It should be noted that in reality, however, these additional solid fillings destroy the idealised point- or line-contact condition and reduce the structure porosity and surface area density. Consequently the fluid flow behaves differently near the region and heat transfer performance may differ as well owing to the additional solid conduction and reduced convection surface area. To investigate this effect, a specially created geometry is numerically simulated and the predictions are compared with those obtained using the simplified geometry. This would be further discussed in the mesh generation section.

3.2. Governing equations and boundary conditions

For convenience of numerical simulations, a geometrical area shown in Fig. 5a is chosen as the computational domain and analysed in the Cartesian coordinates (x, y, z). Let x be the coordinate in the flow direction, y in the direction of channel height (H) and z in the direction

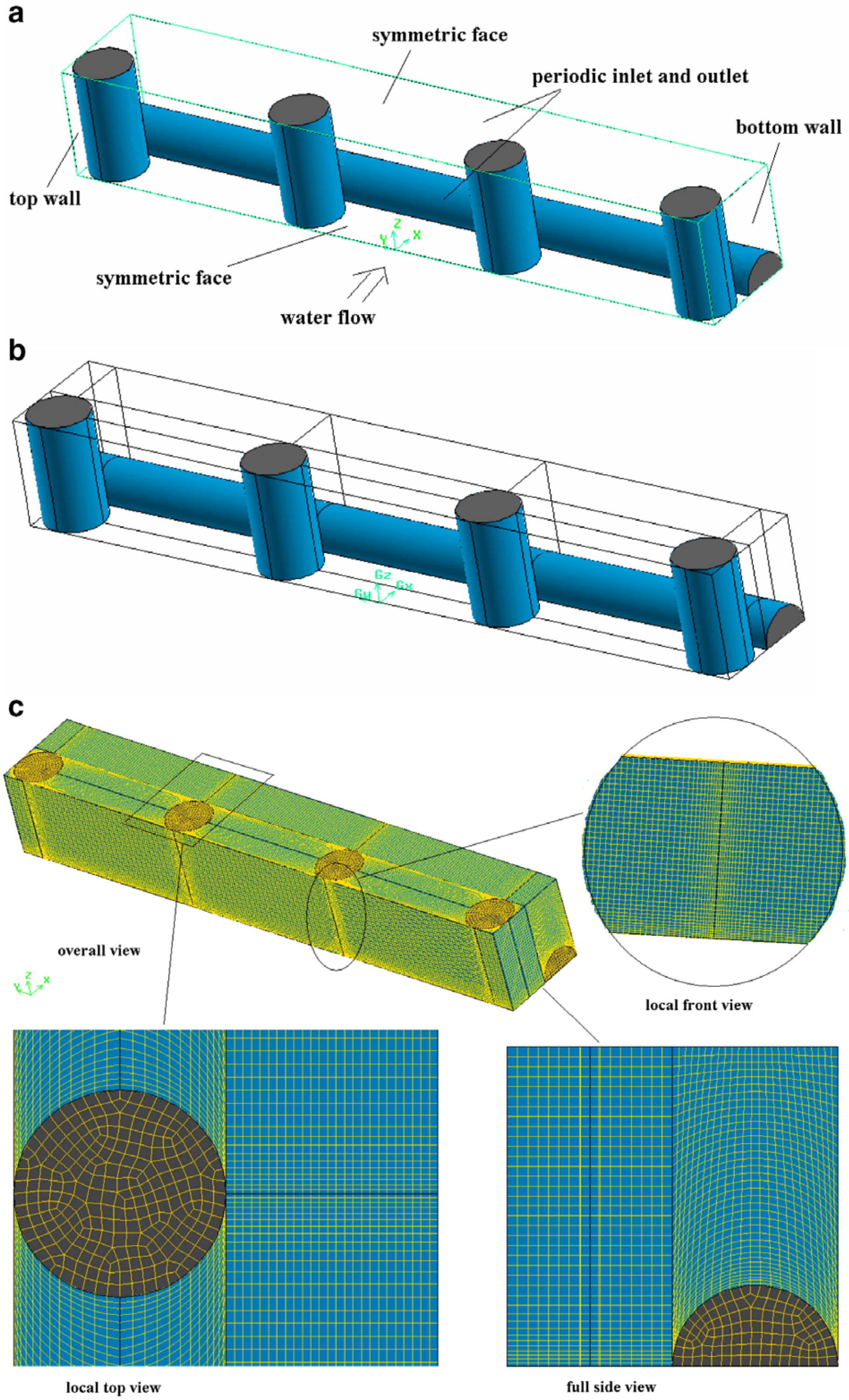

Fig. 5. Computation domain and meshing: (a) chosen computation domain, (b) blocking strategy for meshing and (c) typical resulted mesh.

of channel width (W). The mathematical descriptions of the problem are given as:

3.2.1. Governing equations

Continuity equation for the fluid phase

$$\frac{\partial u_i}{\partial x_i} = 0 \tag{11}$$

Momentum equations for the fluid phase

$$\rho_f u_j \frac{\partial u_i}{\partial x_j} = -\frac{\partial p}{\partial x_i} + \mu \frac{\partial^2 u_i}{\partial x_j \partial x_j} \tag{12}$$

Energy equation for the fluid phase

$$\rho_f c_{pf} u_i \frac{\partial T_f}{\partial x_i} = k_f \frac{\partial^2 T_f}{\partial x_i^2} \tag{13}$$

Energy equation for the solid phase

$$\frac{\partial^2 T_s}{\partial x_i^2} = 0 \tag{14}$$

In Eqs. (11)–(14), x_i refers to the Cartesian coordinates; u_i (or u_j), p and T are velocity, pressure and temperature respectively, with $i, j = 1, 2, 3$ the Einstein notation indices and subscripts f and s denoting fluid and solid phases, respectively.

3.2.2. Boundary conditions

Front and rear symmetric boundaries

$$\left.\frac{\partial \phi}{\partial z}\right|_{z=0,z=W} = 0 \tag{15}$$

where $\phi = (u_i, p, T)$.

Inlet and outlet periodic boundaries

$$\begin{gathered} u_i|_{x=0} = u_i|_{x=L}, \quad \left.\frac{\partial T}{\partial x}\right|_{x=0} = \left.\frac{\partial T}{\partial x}\right|_{x=L}, \\ \rho_f \int_0^W \int_0^H u \, dy \, dz = \dot{m} \end{gathered} \tag{16}$$

Top and bottom facesheets

$$\begin{gathered} u_i|_{y=\pm\frac{H}{2}} = 0, \quad \left.\frac{\partial T}{\partial y}\right|_{y=\frac{H}{2}} = 0, \\ -k_f \left.\frac{\partial T_f}{\partial y}\right|_{y=-\frac{H}{2}} = -k_s \left.\frac{\partial T_s}{\partial y}\right|_{y=-\frac{H}{2}} = q \end{gathered} \tag{17}$$

Interfacial area between solid and fluid phases

$$\begin{gathered} u_i|_{\text{int}} = 0, \quad T_{f,\text{int}} = T_{s,\text{int}}, \\ T_{f,\text{int}} = T_{s,\text{int}}, \quad k_f \left.\frac{\partial T_f}{\partial n}\right|_{\text{int}} = k_s \left.\frac{\partial T_s}{\partial n}\right|_{\text{int}} \end{gathered} \tag{18}$$

where $\boldsymbol{n}$ is the surface normal vector pointing from solid phase to fluid phase.

Note that, for the above mathematical formulation to be valid, the following assumptions need to be introduced:

1. The flow is steady and laminar. The assumption of laminar flow is based on the fact that the maximal Reynolds number based on cylinder diameter considered in the present paper is small (<400).
2. Entrance and exit effects are negligible, i.e., fully developed flow is assumed. This is based on the fact that the entrance and exit regions are short in comparison to the overall channel length for this type of periodic structures [7,29,33].
3. The heat flux entering the solid phase from the bottom facesheet is the same as that entering the fluid phase. A detailed explanation of this assumption can be found in Ref. [28].
4. Natural convection effects are negligible, and so is the radiation heat transfer.
5. The fluid flow is incompressible. The physical properties of both the solid and fluid phases are constant during the temperature range investigated.

3.3. Computation method and mesh generation

A commercially available CFD code, FLUENT™, is employed to simulate the fluid flow and heat transfer within the computational domain. The simulation procedures are

1. the set of governing equations is solved in a segregated fashion, which means that the discretized momentum and energy equations are solved one by one during the iterations;
2. momentum and pressure coupling is handled with SIMPLE algorithm;
3. discretization schemes
   momentum: second-order upwind,
   energy: first-order upwind;
4. Under-relaxation factors
   momentum: 0.2,
   pressure-correction: 0.1,
   energy: 0.4.

To save iteration time, the flow field is obtained first with the energy equation turned off. Once a converged flow field is obtained, the momentum equations are frozen and the energy equation is turned on for further iterations. For the present case, this approach saves the computation time up to 30%.

Meshing is handled with GAMBIT™. The multi-block strategy is used to generate hexahedral-element dominant mesh that is favourable for CFD simulations. A typical blocking strategy is shown in Fig. 5b, with the corresponding mesh shown in Fig. 5c. To resolve flow near solid surfaces, boundary layers attached to the solid surfaces are simulated with sufficiently fine meshes pointing outwards to the fluid phase. It should be noted that the periodic boundary pairs should be specified before the volumes are meshed.

A mesh sensitivity study is carried out, with the input heat flux fixed at 1.2×10^6 W/m^2, same as the experimental condition. Three mesh densities are considered, with 0.409, 1.12 and 2.334 million cells used, respectively. The calculated overall pressure drop and Nusselt number for each case are plotted as functions of Reynolds number in Figs. 6 and 7. For comparison, experimental measurements are also included. In addition, two coefficients are calculated along strut surfaces, at a specified mass flow rate: the averaged skin friction coefficient c_{int} and the surface heat transfer coefficient h_{int}:

$$c_{\text{int}} = \frac{\tau_{\text{int}}}{\frac{1}{2}\rho_{\text{ref}} v_{\text{ref}}^2} \tag{19}$$

$$h_{\text{int}} = \frac{q_{\text{int}}}{T_{\text{int}} - T_{\text{ref}}} \tag{20}$$

where τ_{int}, q_{int} and T_{int} are the shear stress, convective heat flux and area-averaged solid phase temperature at the cylindrical surface, and ρ_{ref}, v_{ref} and T_{ref} are the reference fluid density, mean velocity, and bulk mean temperature respec-

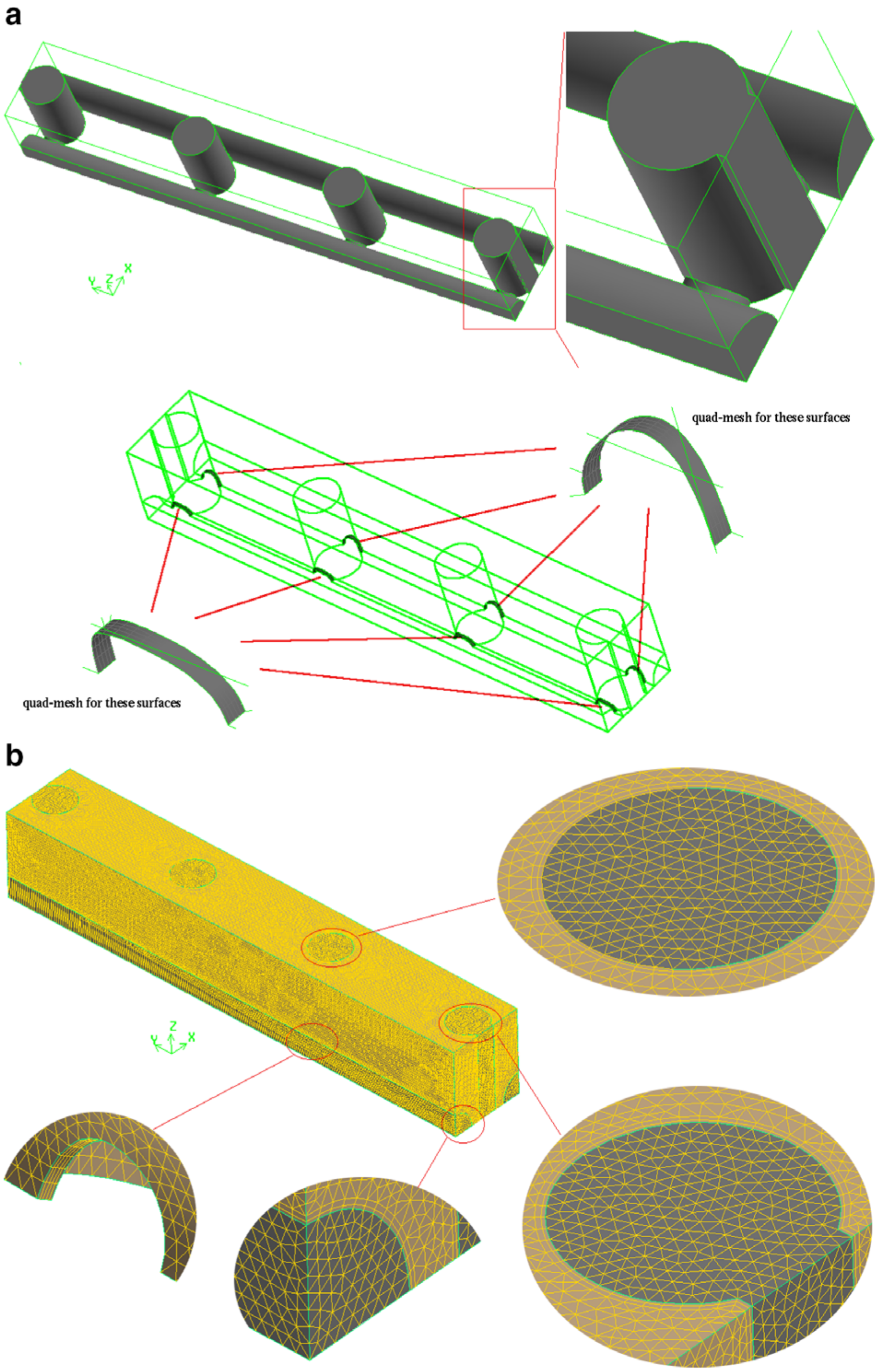

Fig. 6. Computation domain and meshing for geometry with solid fillings around joints: (a) chosen computation domain, (b) typical mesh.

tively. For this study, the reference values are taken at the inlet. The strut surface friction contributes partially to the overall pressure drop over the wire-screen mesh structure, while the surface heat transfer coefficient addresses the energy communication between the solid and fluid phases. Therefore these two coefficients can be used to judge the mesh independence of simulation results. The simulated results for all three cases are summarised in Table 3.

From Figs. 6 and 7 (validation against experiment) and Table 3 (comparison amongst different meshes), it can be seen that a mesh configuration with 1.12 million cells is sufficiently dense and also economical for the present study. It is worth noting that the interfacial heat transfer coefficients in Table 3 address the heat transfer efficiency between the solid and fluid phases. In the present study, the net energy goes from the solid struts to the coolant. As the periodic

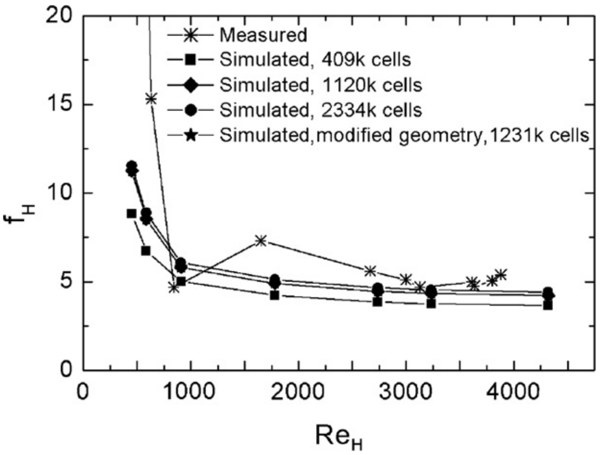

Fig. 7. Frictional factor versus Reynolds number at porosity of 0.795 for experiments and 0.801 for simulations.

Table 3
Results from mesh sensitivity study at $u_m = 0.3165$ m/s ($Re_H = 3250$ for simulations and $Re_H = 3168$ for experiments)

Total number of cells ($\times 10^3$)	409	1120	2334
Friction factor (measured value, 4.69 m^{-1})	3.75	4.43	4.53
Nusselt number (measured value, 252.1)	210.8	238.5	246.2
Interfacial skin friction coefficient, m^{-1}	0.2093	0.2129	0.2141
Interfacial surface heat transfer coefficient, W m^{-2} K^{-1}	1232.4	1267.3	1281.2

boundary condition indicates, the energy going out from the computation domain due to the upstream conduction equals to that coming into the domain due to the conduction at downstream boundary, i.e., the net energy for upstream and downstream boundaries due to conduction is zero. Also it can be derived from the energy balance within the solid volume that the net energy transferred from struts to the coolant is equal to the energy conducted into the struts from the bottom facesheet. As the bulk mean temperature of fluid phase increases along the flow direction from the upstream to downstream, meaning the coolant carries a certain amount of net energy away. The amount energy quantitatively is the summation of energy transferred in from the bottom facesheet owing to fluid convection and solid conduction. The overall averaged heat transfer coefficient at the bottom facesheet can be calculated from Eq. (4), using the known values of Nusselt number in Table 3. Consequently it can be seen that the interfacial surface heat transfer coefficients are much smaller than the overall averaged ones (around 8–10%). This reveals that at the bottom facesheet the heat going into the domain due to convection is much larger that that due to the solid conduction. The probable reasons for this are that (1) the fluid area is much larger than the solid area at the facesheet and (2) the fluid convection relatively efficient compared to the solid conduction despite of the highly different heat conductivities.

As previously discussed, the effect of additional solid fillings around strut joints (and the position where wires contact bottom and top facesheets) on fluid flow and heat transfer is also investigated. The volumes of these fillings are chosen to be sufficiently small so that the reduction in structure porosity is less than 0.39%, and the reduction in surface area density is less than 0.57%. Although the change in geometry is small, these additional solid volumes introduce substantial difficulties in mesh generation. Due to the presence of the solid fillings, it is no longer possible to use the current meshing tools to create an all-hex-cell

Table 4
Parameters used in the numerical simulations

Mean inlet velocity, u_m (m s^{-1})	Heat flux at bottom wall, q (W m^{-2})	Material conductivities, k (W m^{-1} K^{-1})		Heat capacity multiplied by density, ρc_p (J m^{-3} K^{-1})		Porosity, ε
		Fluid	Solid	Fluid	Solid	
0.044125	250,000	0.6	387.6	4,174,472	3,420,618	0.8012
0.044125	12,500	0.6	387.6	4,174,472	3,420,618	0.8012
0.060056	400,000	0.6	387.6	4,174,472	3,420,618	0.8012
0.088749	400,000	0.6	387.6	4,174,472	3,420,618	0.8012
0.173976	560,000	0.6	387.6	4,174,472	3,420,618	0.8012
0.281037	1,000,000	0.6	387.6	4,174,472	3,420,618	0.8012
0.316105	1,200,000	0.6	387.6	4,174,472	3,420,618	0.8012
0.422182	1,100,000	0.6	387.6	4,174,472	3,420,618	0.8012
0.422182	110,000	0.6	387.6	4,174,472	3,420,618	0.8012
0.316105	1,200,000	0.6	202.4	4,174,472	3,420,618	0.8012
0.316105	1,200,000	0.6	120.0	4,174,472	3,420,618	0.8012
0.316105	1,200,000	0.6	60.0	4,174,472	3,420,618	0.8012
0.316105	1,200,000	0.6	19.38	4,174,472	3,420,618	0.8012
0.316105	1,200,000	0.6	202.4	4,174,472	4,174,472	0.8012
0.316105	1,200,000	0.6	202.4	4,174,472	4,034,914	0.8012
0.316105	1,200,000	0.6	202.4	4,174,472	2,368,249	0.8012
0.316105	1,200,000	0.6	202.4	4,174,472	2,087,236	0.8012
0.316105	1,200,000	0.6	387.6	4,174,472	3,420,618	0.7756
0.316105	1,200,000	0.6	387.6	4,174,472	3,420,618	0.8429
0.316105	1,200,000	0.6	387.6	4,174,472	3,420,618	0.8691

mesh for the region near the peak-to-peak nodes and the region where a wire is in contact with the facesheet. Also, a few layers of prism-cells have to be created over the solid wall growing inwards to the fluid volumes, so that the artificial diffusion caused by tetrahedral cells can be limited within an acceptable level. The chosen computational domain and generated mesh for the new geometry are shown in Fig. 6a and b, respectively. A different domain from the one depicted in Fig. 5 was chosen in favour of an easier mesh generation and boundary treatment (mainly for periodic boundary pairs at upstream and downstream). Different mesh densities for this geometry are also evaluated to ensure the converged solutions are mesh insensitive. It has been established that a mesh of about 1.2 million cells is sufficiently dense to obtain satisfactory solutions. The corresponding results are shown in Figs. 6 and 7 together with those predicted using the simplified geometry of Fig. 5 without considering effect of additional solid fillings. It is seen from these results that the effect of solid fillings on both the friction factor and overall Nusselt number is small. Consequently, for the rest of this study, only results obtained with the simplified mesh geometry of Fig. 5 will be presented.

3.4. Simulated cases

The following topics are covered in the present numerical study:

(1) Pressure drop across the wire-screen mesh with varying Reynolds numbers at different porosities.
(2) Variation of average Nusselt numbers with different Reynolds numbers, porosities, solid–fluid properties (mainly k and ρc_p).
(3) Interfacial heat transfer coefficients for different porosities and different solid–fluid properties.

The parameters used in the simulated cases are summarised in Table 4. To change the porosity of the structure, the strut diameter is fixed whilst the channel height was slightly changed so that the number of horizontal wires present in the cross-flow direction (i.e., four wires in this study) remains the same.

4. Experimental results for numerical validations

4.1. Pressure drop

The measured friction factors of the test sample are plotted in Fig. 6 in the Reynolds number range of 440–4000. The simulated data for the simplified geometry with parameters listed in Table 2, using different mesh densities, are also plotted in the same figure, with Reynolds numbers in the range of 500–4500.

From Fig. 6, it can be seen that the friction factor is more or less constant once the Reynolds number exceeds 2500. This indicates that the pressure loss is mainly attributed to the form drag, and interfacial friction becomes less important. The simulated results clearly capture the trend. For higher Reynolds numbers (>2500), the predicted friction factors are slightly smaller than the measured values, but the deviations are reasonable bearing in mind the geometry difference between experiments and simulations and the uncertainty/error in experiments/simulations.

The predicted friction factors with the modified geometry, i.e., with solid fillings around joints shown in Fig. 6a, are plotted in Fig. 7 as functions of the Reynolds number. It can be seen that the pressure lose calculated is almost identical to that for the simplified geometry shown in Fig. 5a. This again attributes to the fact that the pressure lose is mainly caused by the form drag and the fact that the filled solid volumes are added to the area where flow is nearly stagnant and the surface friction is negligible.

4.2. Heat transfer

Similarly, the heat transfer performance of all the copper structures is compared in Fig. 8, where both the Nusselt number and Reynolds number are based on the channel height. It is seen that as the Reynolds number is increased, the Nusselt number increases rapidly at small Reynolds numbers (<1000); at higher Reynolds numbers (>2000), the Nusselt number appears to increase linearly with increasing Reynolds number. The porosity of wire screen structure tested in this study, 0.795, is significantly smaller than that of high porosity metal foams (>0.9) but much larger than that of packed beds. Conduction through solid ligaments is therefore more important in brazed wire screens than that in metal foams (as well as that in packed beds without brazing), especially with high conductivity materials (pure copper in current study) [6]. The overall heat transfer includes forced convection through wire screens, conduction through substrates as well as wire screens.

On average, the simulated Nusselt numbers are larger than test data. However, at higher Reynolds numbers

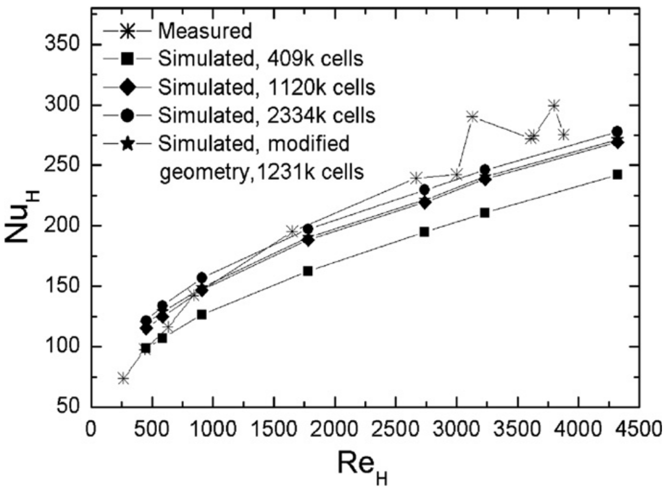

Fig. 8. Nusselt number versus Reynolds number at porosity of 0.795 for experiments and 0.801 for simulations.

(>1500), the predictions appear slightly smaller than measurements. The likely reason could be that at low Reynolds numbers the adiabatic requirement of the whole test section is difficult to maintain in the experiments. Also, at low Reynolds numbers, solid conduction is important; as the Reynolds number increases, convection becomes dominant. Consequently, the fixed set of mesh in fluid volumes may be too dense for low Reynolds number (which then introduces too much artificial diffusion) and not fine enough for high Reynolds number. It should also be noted that at high Reynolds numbers the test data have bigger oscillations. It is likely that the values obtained with the temperature probes become unstable as the flow may have instability behaviour to some extent at high Reynolds numbers.

The calculated Nusselt numbers for the modified geometry are slightly higher than those calculated for the simplified geometry, at the same level of mesh density. This is reasonable because the additional solid volumes improve solid conduction and help heat spreading in solid volumes. Consequently, the overall energy communication between the fluid and solid phases becomes more efficient. However, the difference is small. This may be attributed to the fact that, for the studied wire screen structures, both the wire diameter and channel height are small, and hence the energy transfer between touched wires through heat conduction is less important compared with energy communication between fluid and solid phases.

5. Results and discussion

5.1. Pressure drop against different Reynolds numbers

At the porosity level of 0.801, the predicted friction factor f_H, defined as in Eq. (2), is plotted in Fig. 7 as a function of the Reynolds number. Notice that the results of Fig. 7 can be correlated as $f_H = 114.02 \times Re_H^{-0.3753}$; the coefficient 0.3753 is close to that (i.e., 0.332–0.401) obtained by Zukauskas [32] for a cylinder bank of stagger arrangement. This suggests that the pressure drop behaviour of flow across wire-screen structures is similar to that across banks of staggered cylinders.

It is generally desirable for a compact heat sink to dissipate as much heat and require as little pumping power as possible. From Figs. 7 and 8, it can be seen that when the Reynolds number is increased over a certain value (e.g., around 2000 for the studied cases), the pressure loss becomes more or less constant while the overall Nusselt number still increases quickly. This indicates that high performance wire-screen heat sinks should be designed for Reynolds numbers larger than about 2000 to minimize the pumping power required.

5.2. Overall Nusselt number

The predicted overall Nusselt numbers are plotted in Figs. 8–11 for different material combinations. Fig. 8 plots the averaged Nusselt number as a function of Reynolds number, at a porosity of 0.801. Figs. 9 and 10 address the effect of varying solid–fluid conductivity ratio and heat capacity ratio on the Nusselt number, respectively. With the Reynolds number fixed, Fig. 11 plots the Nusselt number for different porosity levels of copper textiles at a given Reynolds number of 3250.

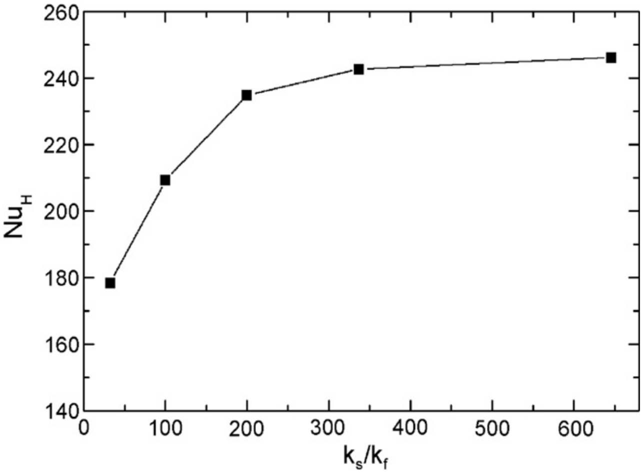

Fig. 9. Nusselt number versus solid–fluid conductivity ratio at porosity of 0.801 and Reynolds number of 3250.

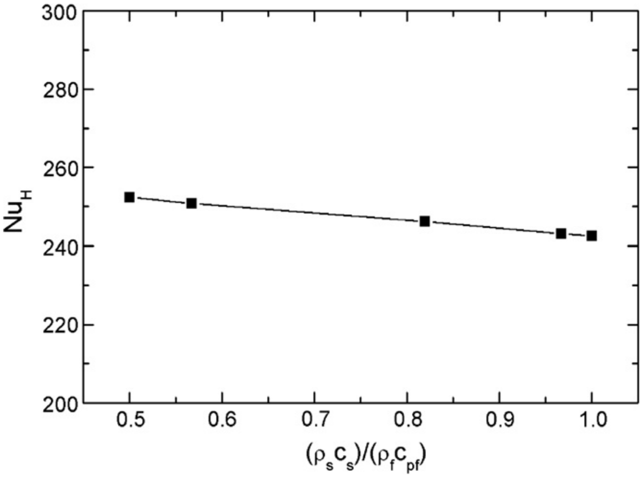

Fig. 10. Nusselt number versus solid–fluid heat capacity ratio at porosity of 0.801 and Reynolds number of 3250.

From Fig. 8, the averaged Nusselt number can be correlated as $Nu_H = 11.56 \times Re_H^{0.374}$. From Fig. 9, it is seen that the heat transfer performance of wire-screen structures is improved with the use of high conductivity materials. However, it seems that there exists a critical solid-to-fluid conductivity ratio above which the value of the Nusselt number changes little. This conductivity ratio, for $\varepsilon = 0.801$, $Re_H = 3250$ and $(\rho_s c_c)/(\rho_f c_{pf}) = 0.8194$, is about 250 (Fig. 9). The ratio of solid–fluid heat capacity ratio also has effect on the heat transfer performance of wire-screen structures (Fig. 10), but this effect is not as pronounced as due to the conductivity ratio: generally the overall

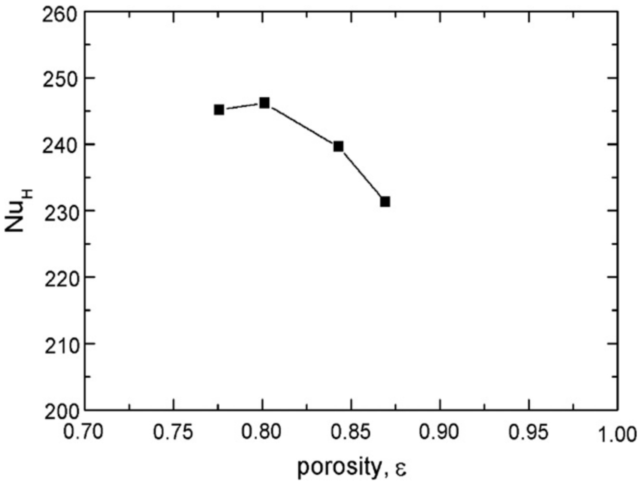

Fig. 11. Nusselt number versus porosity at Reynolds number of 3250 for copper textiles.

Nusselt number slightly decreases as the solid–fluid heat capacity ratio increases.

Fig. 11 shows that the impact of the structure porosity is significant. It appears that there is an optimal porosity near 0.8 (for $k_s/k_f = 646$, $(\rho_s c_c)/(\rho_f c_{pf}) = 0.8194$ and $Re_H = 3250$) in which the overall heat transfer shows the best performance. The decrease of the porosity is due to the thickening of wire struts, which leads to greater flow acceleration due to the blockage by the thickened struts. Then, this flow acceleration increases the heat transfer in both endwall and strut surfaces. However, a further decrease of the porosity causes an increase of the thermally less-active dead flow region at the downstream side of the struts, leading to an overall reduction in the heat transfer. Jing et al. [6] pointed out that, for forced air convection across wire screens, there exists an optimised porosity around 0.7–0.8 for maximal heat dissipation. For open-cell metal foams, Zhao et al. [28] also reported the existence of such an optimal porosity and further claimed that this porosity varies as flow configuration changes, e.g., it increases as the Reynolds number is increased.

6. Conclusions

The overall pressure drop and heat transfer of sandwich structures having brazed metallic textile cores have been both experimentally and numerically investigated under steady-state forced water convection conditions. Uniform heat flux boundary condition is utilised.

For the range of Reynolds numbers considered, fluid flow in all the textile structures is form dominated: the frictional factor is nearly independent of the coolant velocity when Reynolds number exceeds 2000. The frictional factor based on channel height is well correlated to the Reynolds numbers within this range. The correlation is similar to that found for staggered cylinder arrays.

The transport of heat across wire-screen meshes depends on two competing mechanisms: solid conduction and forced convection. At a given Reynolds number, the porosity and surface area density are two key parameters controlling heat transfer. At a given porosity, heat dissipation rate increases as the surface area density is increased. With increasing porosity, the influence of solid conduction decreases while convection increases. Consequently, there exists an optimal porosity (~0.8) for maximal heat dissipation for a given Reynolds number.

The influence of material properties on the overall heat transfer performance of wire-screen structures is significant. In general, a higher solid–fluid conductivity ratio results in higher heat dissipation. However, the change is insignificant when the conductivity ratio exceeds a critical value (~250 for the studied cases). The effect of solid–fluid heat capacity ratio is not as pronounced as the thermal conductivity ratio.

Acknowledgements

The authors wish to thank the National Basic Research Program of China through Grant No. 2006CB601202, the National Natural Science Foundation of China through Grant Nos. 10328203 and Grant No. 10572111, the National 111 Project of China (Grant No. B06024), and the US Office of Naval Research (ONR) for partial financial support of this work. The test rig for pressure drop and heat transfer measurements was provided by Professor P.X. Jiang at Department of Thermal Engineering, Tsinghua University, China.

References

[1] U. Bin-Nun, D. Mantitakos, Low cost and high performance screen laminate regenerator matrix, Cryogenics 44 (2004) 439–444.
[2] A. Kolb, E.R.F. Winter, R. Viskanta, Experimental studies on a solar collector with metal matrix absorber, Solar Energy 65 (1999) 91–98.
[3] N.S. Tharur, J.S. Saini, S.C. Solanki, Heat transfer and friction factor correlations for packed bed solar air heater for a low porosity system, Solar Energy 74 (2003) 319–329.
[4] P.J. Richards, M. Tobinson, Wind loads on porous structure, J. Wind Eng. Ind. Aerodyn. 83 (1999) 455–465.
[5] A. Bejan, S.L. Kim, A.I.M. Morega, S.W. Lee, Cooling of stacks of plates shielded by porous screens, Int. J. Heat Fluid Flow 16 (1994) 16–24.
[6] J. Tian, K. Kim, T.J. Lu, H.P. Hodson, D.T. Queheillant, D.J. Sypeck, H.N.G. Wadley, The effects of topology upon fluid-flow and heat-transfer within cellular copper structures, Int. J. Heat Mass Transfer 47 (2004) 3171–3186.
[7] T. Kim, Fluid-flow and heat-transfer in a lattice-frame material, Ph.D. thesis, Department of Engineering, University of Cambridge, 2003.
[8] S. Ergun, Fluid flow trough packed columns, Chem. Eng. Prog. 48 (1952) 89–94.
[9] J.C. Armour, J.N. Cannon, Fluid flow through woven screens, AIChE J. 14 (1968) 415–421.
[10] J.R. Sodre, J.A.R. Parise, Friction factor determination for flow through finite wire-mesh woven-screen matrices, ASME J. Fluid Eng. 119 (1997) 847–851.
[11] C.T. Hsu, K.W. Wong, P. Cheng, Effective stagnant thermal conductivity of wire screen, J. Thermophys. 10 (1996) 542–545.

[12] R.A. Wirtz, J. Xu, J.W. Park, D. Ruch, Thermal/fluid characteristics of 3D woven mesh structures as heat exchanger surfaces, IEEE Trans. Compon. Packag. Technol. 26 (2003) 40–47.
[13] J. Xu, R.A. Wirtz, In-plane effective thermal conductivity of plain-weave screen laminates, IEEE Trans. Compon. Packag. Technol. 25 (2002) 615–620.
[14] W.S. Chang, Porosity and effective thermal conductivity of wire screens, ASME J. Heat Transfer 112 (1990) 5–9.
[15] B. Paul, J.S. Saini, Optimization of bed parameters fro packed bed solar energy collection system, Renew. Energy 29 (2004) 1836–1876.
[16] M.L. Hunt, C.L. Tien, Effect of thermal dispersion on forced convection in fibrous media, Int. J. Heat Mass Transfer 31 (1988) 301–309.
[17] K. Vafi, S.J. Kim, Forced convection in a channel filled with a porous medium: an exact solution, ASME J. Heat Transfer 111 (1989) 1103–1106.
[18] A. Amiri, K. Vafai, Transient analysis of incompressible flow through a packed bed, Int. J. Heat Mass Transfer 41 (1998) 4259–4279.
[19] B. Alazmi, V. Vafai, Analysis of variants within the porous media transport models, ASME J. Heat Transfer 122 (2000) 303–326.
[20] A.V. Kuznetsov, A perturbation solution for heating a rectangular sensible heat storage packed bed with a constant temperature at the walls, Int. J. Heat Mass Transfer 40 (1997) 1001–1006.
[21] K. Muralidhar, K. Suzuki, Analysis of flow and heat transfer in a regenerator mesh using a non-Darcy thermally non-equilibrium model, Int. J. Heat Mass Transfer 44 (2001) 2493–2504.
[22] F. Duprat, G. Lopez, Comparison of performance of heat regenerators: relation between heat transfer efficiency and pressure drop, Int. J. Energy Res. 25 (2001) 319–329.
[23] A. Ahmad, J. Saini, H. Varma, Effect of geometrical and thermophysical characteristics of bed materials on the enhancement of thermal performance of packed-bed solar air heaters, Energy Convers. Manage. 36 (1995) 1185–1195.
[24] M. Ozdemir, A.F. Ozguc, Forced convective heat transfer in porous medium of wire screen meshes, Heat Mass Transfer 33 (1997) 129–136.
[25] D. Mehta, M.A. Hawley, Wall effect in packed columns, I&EC Process Des. Dev. 8 (1969) 280–282.
[26] K. Vafai, Convective flow and heat transfer in variable-porosity media, J. Fluid Mech. 147 (1984) 233–259.
[27] M. Ozdemir, A.F. Ozguc, Porosity variation and determination of REV in porous medium of screen meshes, Int. Commun. Heat Mass Transfer 24 (1997) 955–964.
[28] C.Y. Zhao, T. Kim, T.J. Lu, H.P. Hodson, Modelling on thermal transport in cellular metal foams, AIAA J. 3014 (2002) 1–11.
[29] T. Kim, H.P. Hodson, T.J. Lu, Fluid flow and endwall heat-transfer characteristics of lattice-frame materials, Int. J. Heat Mass Transfer 47 (2004) 1129–1140.
[30] T. Kim, C.Y. Zhao, T.J. Lu, H.P. Hodson, Convective heat dissipation with lattice-frame materials, Mech. Mater. 36 (2004) 767–780.
[31] H.W. Coleman, W.G. Steele, Experimentation and Uncertainty Analysis for Engineers, second ed., John Wiley, New York, 1999.
[32] Zukauskas, Convective heat transfer in cross flow, in: S. Kakac, R.K. Shah, W. Aung (Eds.), Handbook of Single-Phase Convective Heat Transfer, John Wiley, New York, 1987.
[33] J. Xu, H.P. Hodson, T.J. Lu, A numerical study on wire-screen mesh with complicate geometry, in preparation.

Further reading

[1] T. Kim, A.J. Fuller, H.P. Hodson, T.J. Lu, An experimental study on thermal transport in lightweight metal foams at high Reynolds numbers, in: Proceedings of International Symposium of Compact Heat Exchangers, Grenoble, France, 2002, pp. 227–232.
[2] J. Tian, Fluid flow and heat transfer in woven textiles, Ph.D. thesis, Department of Engineering, University of Cambridge, 2005.